Research article

Jaehak Lee[a], Suyeon Yang[a], Jihye Lee, Jun-Hyuk Choi, Yong-Hee Lee, Jung H. Shin[b] and Min-Kyo Seo*

Extraordinary optical transmission and second harmonic generation in sub–10-nm plasmonic coaxial aperture

https://doi.org/10.1515/nanoph-2020-0066
Received January 30, 2020; revised March 17, 2020; accepted March 19, 2020

Abstract: Recent development in nanofabrication technology has enabled the fabrication of plasmonic nanoapertures that can provide strong field concentrations beyond the diffraction limit. Further utilization of plasmonic nanoaperture requires the broadband tuning of the operating wavelength and precise control of aperture geometry. Here, we present a novel plasmonic coaxial aperture that can support resonant extraordinary optical transmission (EOT) with a peak transmittance of ~10% and a wide tuning range over a few hundred nanometers. Because of the shadow deposition process, we could precisely control the gap size of the coaxial aperture down to the sub–10-nm scale. The plasmonic resonance of the SiN_x/Au disk at the center of the coaxial aperture efficiently funnels the incident light into the sub–10-nm gap and allows strong electric field confinement for efficient second harmonic generation (SHG), as well as EOT. In addition to the experiment, we theoretically investigated the modal properties of the plasmonic coaxial aperture depending on the structural parameters and correlation between EOT and SHG through finite-difference time-domain simulations. We believe that our plasmonic coaxial apertures, which are readily fabricated by the nanoimprinting process, can be a versatile, practical platform for enhanced light–matter interaction and its nonlinear optical applications.

Keywords: plasmonics; gap plasmon; plasmonic coaxial aperture; extraordinary optical transmission; second harmonic generation.

1 Introduction

Owing to the strong light–matter interactions beyond the optical diffraction limit [1–5], plasmonic nanostructures have facilitated various applications such as high-resolution imaging [6], sensors [7], tweezers [8], photovoltaics [9], structural color generation [10, 11], and optical medical therapies [12]. Extraordinary optical transmission (EOT) [13] and second harmonic generation (SHG) [14] have also been attractive applications of subwavelength-scale field concentration of the plasmonic nanostructures. Enabling the incident light to funnel the subwavelength apertures on a thin metallic film and interact with nanometer-scale materials, EOT has been particularly advantageous for the applications to ultrathin color filters [15], highly sensitive optical sensors [16], tunable band perfect absorbers [17], and optical trapping [18]. Meanwhile, SHG, which is prohibited in centrosymmetric materials such as most noble metals, has been observed in carefully designed plasmonic

[a]**Jaehak Lee and Suyeon Yang:** These authors contributed equally to this work.
[b]Deceased September 30, 2016
***Corresponding author: Min-Kyo Seo,** Department of Physics, Korea Advanced Institute of Science and Technology, Daejeon 34141, Republic of Korea, e-mail: minkyo_seo@kaist.ac.kr.
https://orcid.org/0000-0003-0618-3955
Jaehak Lee: Department of Physics, Korea Advanced Institute of Science and Technology, Daejeon 34141, Republic of Korea; and Division of National Supercomputing, Korea Institute of Science and Technology Information, Daejeon 34141, Republic of Korea.
https://orcid.org/0000-0002-3013-9332
Suyeon Yang: Department of Physics, Korea Advanced Institute of Science and Technology, Daejeon 34141, Republic of Korea; and Current address: Department of Physics, Wageningen University and Research Centre, Droevendaalsesteeg 4, 6708 PB Wageningen, the Netherlands
Jihye Lee and Jun-Hyuk Choi: Nanomechanical Systems Research Division, Korea Institute of Machinery and Materials, Daejeon 34103, Republic of Korea
Yong-Hee Lee: Department of Physics, Korea Advanced Institute of Science and Technology, Daejeon 34141, Republic of Korea
Jung H. Shin: Department of Physics, Korea Advanced Institute of Science and Technology, Daejeon 34141, Republic of Korea; and Graduate School of Nanoscience and Technology, Korea Advanced Institute of Science and Technology, Daejeon 34141, Republic of Korea

Open Access. © 2020 Min-Kyo Seo et al., published by De Gruyter. This work is licensed under the Creative Commons Attribution 4.0 Public License.
Published online April 18, 2020

nanostructures that provide local symmetry breaking and high field concentration [19–25]. The resultant half-wavelength light emission and its high sensitivity to the structural changes provide novel applications, from ultrashort-width pulse generations [26, 27] to ultrahigh-sensitive surface morphologies [28, 29]. As their origin is the same, the electric field concentration, EOT, and SHG can be simultaneously created with a strong correlation [30].

Recently, plasmonic coaxial nanoapertures [31, 32] have been suggested as excellent platforms for EOT and its applications [15, 33–35]. In addition, employing the atomic layer deposition [36] or shadow deposition method [37], there has been significant progress in fabricating plasmonic coaxial apertures in a large and scalable area, which is necessary for practical applications such as biosensing [37] and color filters [15]. However, no systematic studies have been reported on the simultaneous creation and correlation of both EOT and efficient SHG in a plasmonic coaxial aperture yet. This is mainly because of the symmetric geometry of the metal–insulator–metal gap of the conventional planar coaxial aperture that cancels the second harmonic polarizations on both surfaces of the gap [14, 38–40]. Moreover, typical coaxial nanoapertures have suffered from rapid changes in the properties of EOT and field concentration, depending on the resonance wavelength [35, 37].

In this work, we demonstrate resonant EOT through a sub–10-nm plasmonic coaxial aperture with asymmetric gap geometry and the resulting enhancement of SHG. The nanoimprint and shadow deposition methods, which are capable of large-scale processing, enabled the precise control of the geometry and gap size of the coaxial aperture in the nanometer scale. Depending on its geometry, the plasmonic coaxial aperture can tune the resonant wavelength of EOT over a wide spectral range of a few hundred nanometers, maintaining the magnitude of EOT. We systematically investigated the interrelationship between EOT and SHG considering the aperture geometry and resonant wavelength. We believe that the simultaneous, high-precision, and broadband controllability of the transmission and the field confinement of our plasmonic coaxial aperture may suggest several potential applications such as ultrasensitive nonlinear plasmonic sensing [41], super-resolution imaging [42], single nanoparticle detection [43], and active metamaterials [44].

2 Results and discussion

Figure 1A–C show the schematic and scanning electron microscope (SEM) images of the plasmonic coaxial aperture structure. The shadow deposition of Au on the SiN_x disk supported by the SiO_2 post forms the plasmonic coaxial aperture with a sub–10-nm air gap along the circumference. We fabricated identical coaxial apertures over a large area (0.5 cm^2) using the nanoimprinting process. The period of the triangular lattice was 800 nm, which is sufficiently large to ignore the coupling between the coaxial apertures, as well as sufficiently small to exclude the diffraction grating effect for the given wavelength range and the numerical aperture (NA) of the employed objective. The plasmonic resonance of the SiN_x/Au disk strongly confines the electric field at the aperture gap and causes EOT and efficient SHG. We experimentally observed that when we pumped multiple apertures each aperture exhibited a bright SHG signal (Figure 1D). Subsequently in this work, we investigated the operation of a single aperture independently.

Figure 1E shows the schematic of the SHG measurement setup. A femtosecond laser with a center wavelength of 1560 nm (FemtoFiber pro NIR; Toptica, Munich, Germany) was focused on the sample by an objective with an NA of 0.65 and a linear polarizer. The spot size of the pump laser was ~1.58 μm. The repetition rate and pulse width were 80 MHz and 100 fs, respectively. The SHG signal radiating to the backside of the sample was collected by another objective (NA = 0.6) and detected by an electron-multiplying charge coupled device (EMCCD) camera (iXon3 897; Andor Technology, Belfast, United Kingdom). To isolate the SHG signal from the pump laser, we employed short-pass (<1300 nm) and band-pass filters (775 ± 25 nm). For the EOT spectra measurements, we employed a collimated beam of a supercontinuum light source (SuperK COMPACT; NKT Photonics, Birkerød, Denmark) and a monochromator coupled with an array detector (AvaSpec-NIR512; Avantes, Apeldoorn, The Netherlands), as shown in Figure 1F.

The detailed fabrication process is described in Figure 2A. First, we deposited an SiN_x (70 nm)/SiO_2 (45 nm)/SiN_x (70 nm) multilayer on the quartz substrate through the radiofrequency (RF) sputtering process. Second, an array of SiN_x nanodisks with a diameter of 200 nm was fabricated by the ultraviolet nanoimprint patterning [45] and reactive ion etching processes. Third, the buffered oxide etchant selectively etched the SiO_2 layer and formed the SiN_x disk supported by the SiO_2 post. Fourth, an additional RF sputtering of SiN_x was performed to increase the height and diameter of the SiN_x disk and control the size of the final Au–air–Au gap. Finally, we conformally deposited the Au layer using the direct current (DC) sputtering process and built the plasmonic coaxial aperture structure in terms of the shadow deposition [46–48].

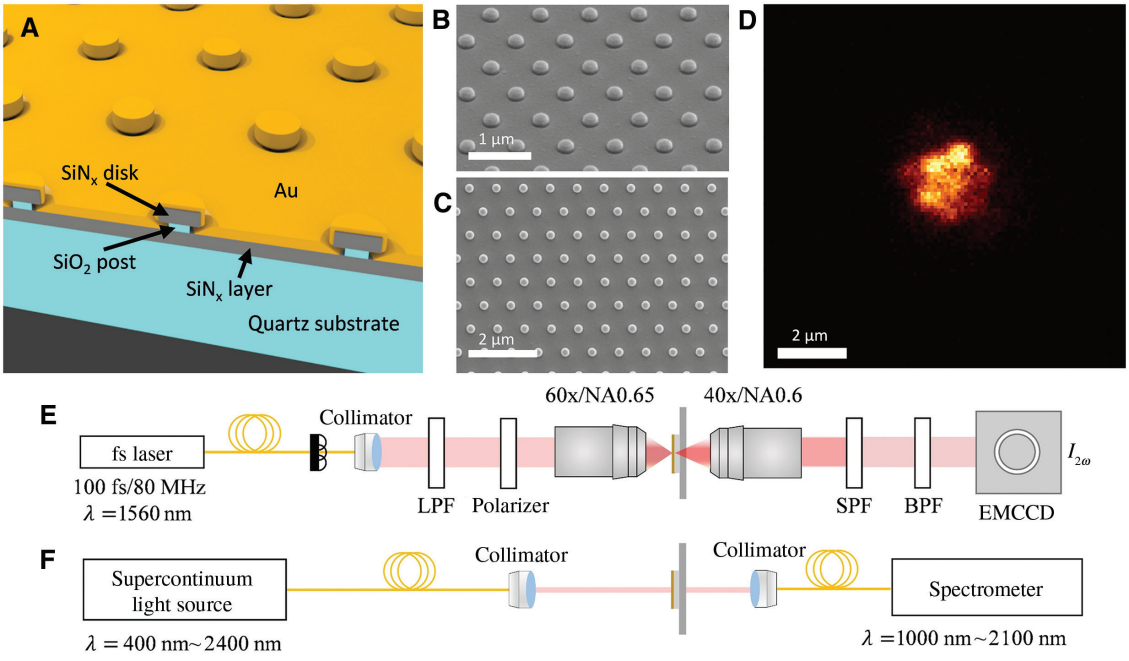

Figure 1: Scheme of the experiment.
(A) Schematics of coaxial plasmonic aperture array. (B) Scanning electron microscope image of a coaxial plasmonic aperture array sample (38° tilted view). (C) Scanning electron microscope image of the sample (top view). (D) Measured EMCCD image of the SHG output radiated from the bottom (substrate side) of the aperture array while pumped from the top (Au side) with 1560-nm femtosecond laser on multiple apertures. The brighter area indicates the higher intensity. (E) Schematic of the SHG measurement setup. (F) Schematic of the EOT measurement setup.

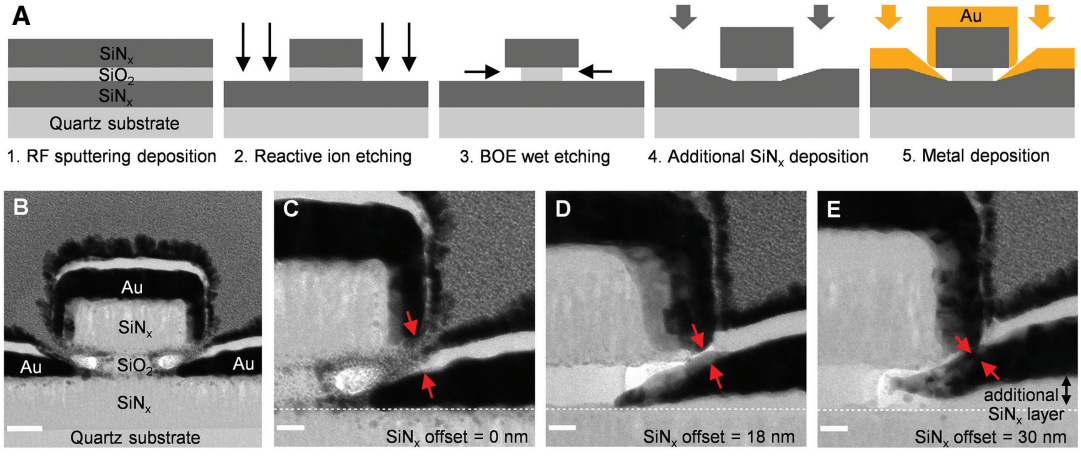

Figure 2: Fabrication of the plasmonic coaxial apertures.
(A) Fabrication process of plasmonic coaxial apertures. Arrows indicate the direction of the processes at each step. (B) Cross-sectional TEM image of a coaxial plasmonic aperture sample without SiN_x offset (scale bar, 50 nm). All samples were sliced using focused ion beam (FIB) milling as ~100-nm thickness before the TEM measurement. The regions without material marks represent protective Cu and Pt layers deposited before the FIB milling. Transmission electron microscope images of the samples with various SiN_x offset thicknesses: (C) 0 nm, (D) 18 nm, and (E) 30 nm each (scale bar, 20 nm). White dashed lines indicate original SiN_x layer surfaces before the additional SiN_x deposition. Red arrows indicate the formation of air gap.

Figure 2B shows a transmission electron microscope (TEM) image of the cross section of the fabricated plasmonic coaxial aperture. The conformal deposition of the Au layer and formation of the sub–10-nm gap can be clearly observed. As shown in the magnified images (Figure 2C–E), the metal–air–metal gap can be controlled from 24 nm to <6 nm depending on the offset by the additional SiN_x layer. We note that the presence of the undercut SiO_2 post

beneath the SiN_x disk enabled the creation of the sub–10-nm scale gap with asymmetric cross-sectional geometry. The conformal DC sputtering deposition allowed the Au layer to penetrate into the undercut area in the form of a tail. The sharp bottom edge of the Au layer deposited on the side wall of the SIN_x disk and the tail of the penetrated Au layer resulted in the nanogap with the asymmetric cross section, which can avoid the effect of second harmonic polarization canceling in symmetric metal–insulator–metal gap structures [14, 38–40].

We theoretically investigated the modal properties of the plasmonic coaxial aperture using the finite-difference time-domain (FDTD) method. Figure 3A shows the calculated field profile of the plasmonic resonant mode. The linearly polarized incidence couples with the plasmonic dipole resonance mode of the Au/SiN_x nanodisk and funnels into the aperture gap, showing strong field confinement. According to the cross-sectional geometry of the aperture, the E_z field dominates in the field confinement. The antisymmetric E_z field distribution with respect to the y-z plane accompanies the symmetric E_x field distribution, which results in the effective coupling to the radiation propagating along the z axis. We can simultaneously control the peak transmittance and center wavelength of the resonance mode, depending on fine structural changes of the Au nanogap, such as the size of the gap and length of the penetrated Au tail, as well as the diameter and height (see also Supplementary Material 1) of the Au/SiN_x nanodisk. The size of the gap is defined as the shortest distance between the Au layers, and the length of the tail is the inclined distance between the gap position and the end of the penetrated Au layer (Figure 3B). In Figure 3C, we calculated the spectral behaviors of coaxial apertures with different gap sizes and tail lengths. In the simulations, the gap and tail varied from 6 to 18 nm and from 18 to 54 nm, respectively. As shown in Figure 3D, the electric field is strongly confined in the gap region, regardless of the structural conditions; this validates our model on the funneling of the incident wave to the gap following the coupling with the plasmonic resonance of the Au/SiN_x disk. As the gap size and tail length decrease, the center wavelength of EOT increases. In contrast, the peak transmittance increases as the gap size increases or tail length decreases. Therefore, by employing the complement effects of the gap size and tail length, we can engineer the properties of EOT with a high degree of freedom.

To examine the field confinement at the gap and its correlation with EOT, we calculated the electric

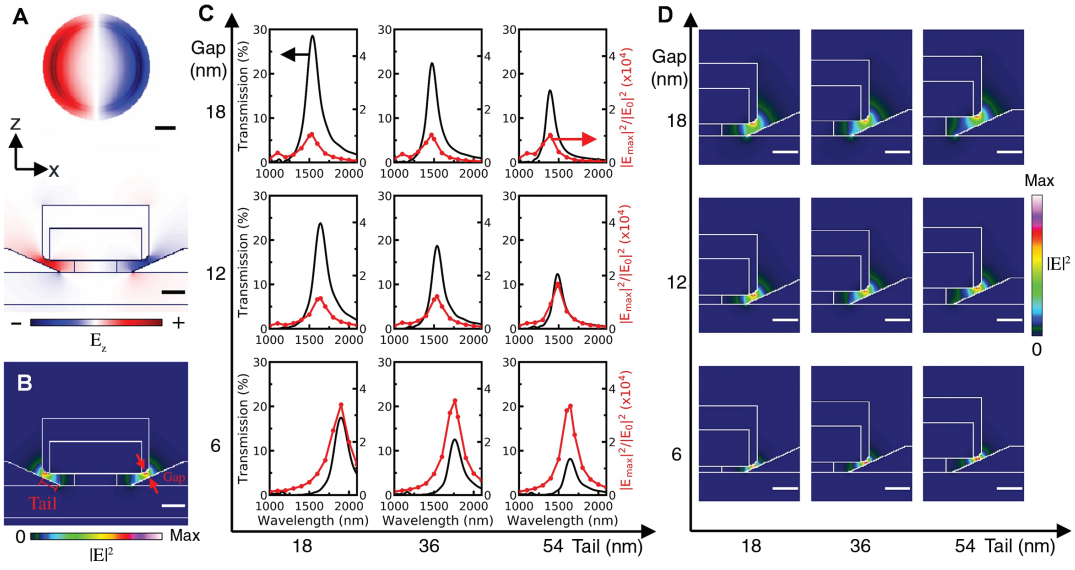

Figure 3: Calculated optical properties according to the aperture geometries.
(A) Electric field distribution of vertical component (E_z) of a plasmonic coaxial aperture at the resonance wavelength calculated using FDTD method. The cross-sectional values were obtained in the horizontal plane along the center of the gap and the vertical plane parallel to the polarization of the source along the center of the aperture (scale bar, 50 nm). Solid lines at the vertical cross-sectional image describe boundaries of different materials. (B) Cross-sectional electric field intensity ($|E|^2$) distribution along the center of the disk of the same structure in (A) (scale bar, 50 nm). (C) Calculated transmission (black solid lines) and electric field enhancement ($|E_{max}|^2/|E_0|^2$, red lines with dots) of plasmonic coaxial apertures with various gaps (6, 12, and 18 nm) and metal tail lengths (18, 36, and 54 nm). (D) $|E|^2$ distributions of the structures in (C) at each resonance wavelength (scale bar, 50 nm). All FDTD simulations were performed using the calculation grids with 2-nm cell sizes and Au collision frequency of 17.1 THz.

field enhancement, $|E_{max}|^2/|E_0|^2$ (red lines with dots in Figure 3C). E_{max} and E_0 are the electric field at maximum and that of the incident light, respectively. The field enhancement shows spectral behavior similar to EOT, confirming that the plasmonic resonance mediates the funneling of the incident light into the subwavelength gap. As shown in the intensity profiles of Figure 3D, the electric field is maximized in the gap region, particularly at the bottom edge of the Au/SiN_x disk. Under the resonant condition, the electric field enhancement is on the order of 10^4. The peak of the field enhancement increased more than threefold as the gap size decreased from 18 nm to 6 nm. In contrast, the tail length effectively tunes the transmission peak, but hardly affects the magnitude of the field enhancement. Here, we note that the electric field concentration at the metal (Au)–air boundary considerably enhances the probability of SHG [23]. Our plasmonic coaxial apertures thus have the advantages of not only strong field concentration depending on the gap size but also wide tunability of the resonance to match with the target wavelength, depending on other structural parameters, tail length, and Au/SiN_x disk size.

Figure 4A and B show the measured and calculated EOT spectra of the demonstrated plasmonic coaxial apertures depending on the offset of the additional SiN_x layer from 0 to 36 nm with a 6-nm step, respectively. The thickness of the Au layer was fixed to 50 nm. The gap size was obtained or extrapolated from the TEM images in Figure 2C–E. Figure 4C shows the cross sections of the simulated plasmonic coaxial apertures and the electric field intensity profiles at the wavelength of 1560 nm. All the samples exhibited well-defined single-mode resonance in transmission, of which the center wavelength was controlled over a very wide spectral range, from 1318 to >2000 nm beyond the measurement range. Meanwhile, the peak transmittance remains ~10% on average in experiments (~15% on average in simulations). As discussed before, the gap size and tail length decrease as the offset of the additional SiN_x layer increases, which constructively boosts the redshift of the resonant wavelength and enables such a wide tuning range. On the other hand, the complementary

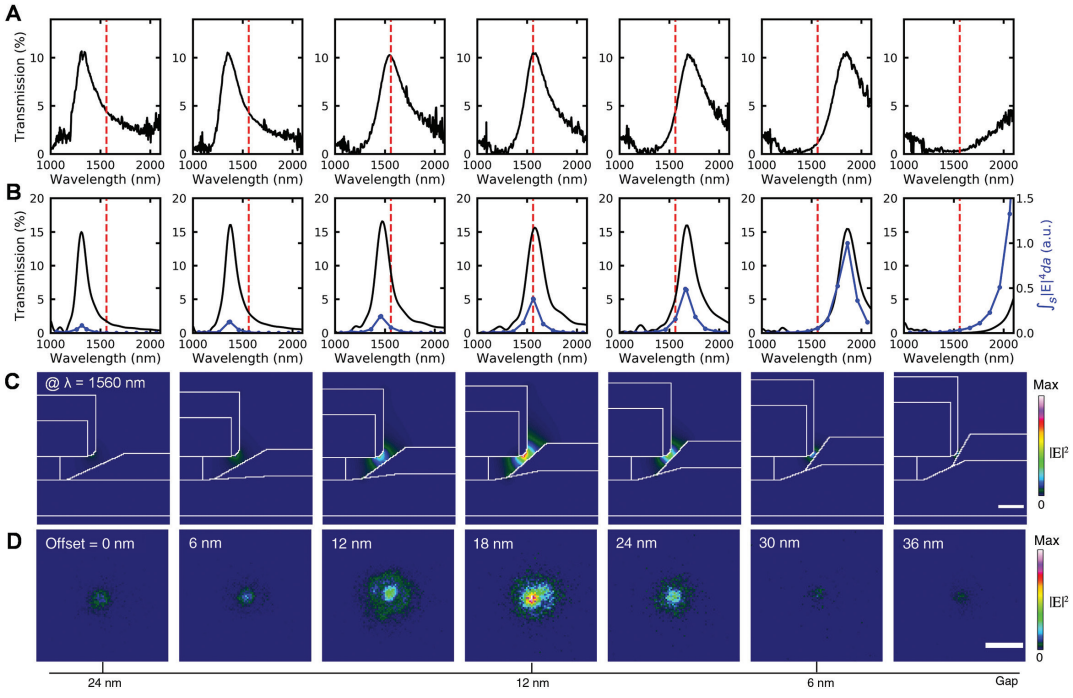

Figure 4: Interrelationship between EOT and SHG.
(A) Experimental transmission spectra of the plasmonic coaxial aperture arrays with various SiN_x offset thicknesses (0, 6, 12, 18, 24, 30, and 36 nm, respectively) and estimated gap sizes with (~24 nm to <6 nm), measured using the setup in Figure 1F. Red dashed lines indicate the pumping wavelength (1560 nm) of the SHG measurement setup. (B) Calculated transmissions (black solid lines) and square sum of the electric field intensity over the metal–air boundary ($\int_S |E|^4\, da$, blue solid lines with dots) for the estimated structures of (A). (C) Calculated cross-sectional $|E|^2$ distribution of each structure under the irradiation of 1560-nm light. White solid lines describe boundaries of different materials (scale bar, 50 nm). (D) Experimental SHG images for the samples of (A), measured from the EMCCD using the setup in Figure 1E (scale bar, 2 μm). On (B–D), the measured or calculated intensity of each structure was normalized by a common coefficient for comparison.

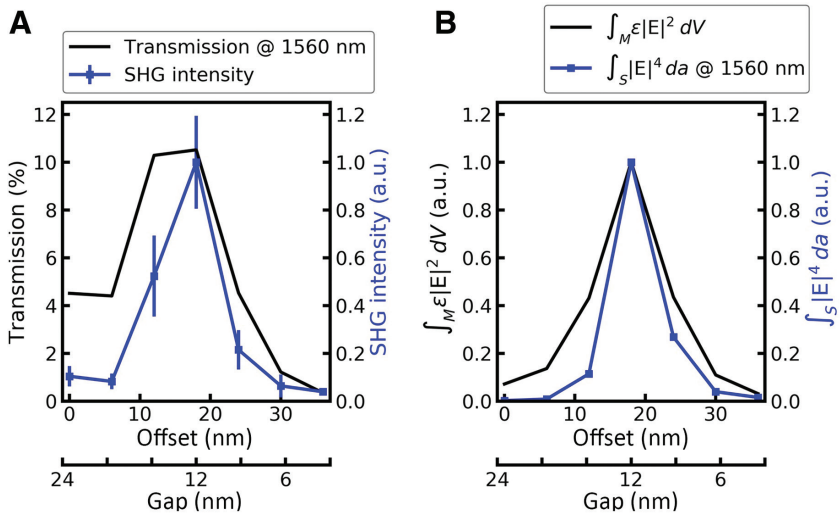

Figure 5: Extraordinary optical transmission and SHG with various SiN_x offsets.
(A) Measured transmissions at 1560-nm wavelength (black solid line) and SHG intensities (blue lines with error bars) of the samples in Figure 4A and D. The error bar of the SHG intensity indicates standard deviations of different measurements. (B) Total electric field energy integrated over the resonance mode ($\int_M \varepsilon |E|^2 \, dV$, black solid line) and square sum of the electric field intensity over the metal–air boundary $\int_S |E|^4 \, da$ (blue lines with squares) at 1560-nm wavelength, for the structures in Figure 4B and C.

behaviors of the gap and tail result in the peak transmittance, independent of the resonant wavelength. The simulation results show a narrower spectral width and a higher peak transmittance than the experimental results. This difference mainly originates from the higher absorption of the structures in the experiments, with multigrained Au layer or fabrication imperfections, than those in the simulations.

We now examine the SHG of plasmonic coaxial apertures in the experiments. Figure 4D shows the measured intensity profiles of SHG from a single plasmonic coaxial aperture activated by the pumping laser with a spot radius of ~790 nm, which is smaller than the period of the triangular lattice. The SHG is maximized when the resonant wavelength in the transmission matches the pumping wavelength (1560 nm). As shown in Figure 4B, the square sum of the electric field intensity over the metal–air boundary, a source key of SHG, exhibits spectral behavior similar to EOT. Indeed, the coupling and funneling of the incident light into the gap area are crucial to SHG. The square sum of the electric field intensity over the metal boundary was at least 10^6 higher than that of a flat Au film (Figure S3). The longer the resonance wavelength, the larger the square sum of the electric field intensity because of the following reasons. First, the smaller gap size causes stronger field confinement, as well as longer resonant wavelength. Second, the larger absolute refractive index of Au at the longer wavelength makes the electric fields at the boundary stronger than those in the interior. Although we here focused on the effect of the fundamental electric dipole contribution on SHG and calculated the square sum of the electric field intensity, we note that the effects of higher-order terms may need to be considered further in nanoscale structures [49–51]. We believe that, supporting high-quality EOT and efficient field confinement, our plasmonic coaxial aperture can be a useful platform for the implementation and application of nonlinear optical phenomena, even in the mid-infrared region [34].

Figure 5 presents the experimental results of EOT and SHG at the wavelength of 1560 nm and compares them with the simulated results. The SHG intensity is more sensitive to structural changes than EOT, and its maximum and minimum differed by ~25 times from the experimental results. It is clearly confirmed that the square sum of the electric field intensity over the metal–air boundary correlates with SHG. Moreover, the electric field concentration in the gap region (see also Figure 4C) successfully represents the behavior of EOT.

3 Conclusions

In summary, we presented plasmonic coaxial apertures supporting EOT and SHG. The shadow deposition method enabled us to reduce the gap size of the

aperture to the sub–10-nm scale. The plasmonic resonance of the SiN_x/Au disk efficiently couples with the incident light and funnels it into the gap area with strong electric field confinement. We experimentally demonstrated resonant EOT with a peak transmittance of ~10% and a wide tuning range of more than several-hundred nanometers. Theoretical modeling based on numerical calculations revealed that the precise control of the length of the penetrated Au tail and the gap size is the key to such a widely tunable, stable generation of EOT. We also realized controllable SHG depending on the structural parameters and investigated its correlation with the square sum of the electric field intensity at the metal–air boundary. We believe that our plasmonic coaxial apertures, which are even compatible with the nanoimprinting process, can be a versatile, practical platform for various applications including nonlinear optical components, functional metasurfaces, and broadband optical sensors.

4 Methods

4.1 Finite-difference time-domain simulation

We employed full-vectorial three-dimensional FDTD simulation to calculate the transmission spectra and the electric field enhancements of the plasmonic coaxial aperture structures. We used a uniform Yee lattice of 2-nm-size unit cells. The Drude model and the recursive convolution method were used to model the permittivity of gold [52]. The periodic boundary condition was applied along the horizontal directions to simulate the array structure in the triangular lattice, and the convolution perfectly matched layers were used at the boundaries of the vertical direction. To calculate the square sum of the electric field intensity for the prediction of SHG, we integrated the square of the electric field intensity only at the outermost grids of the gold media.

Acknowledgments: This work was supported by Basic Science Research Program through the National Research Foundation of Korea funded by the Ministry of Education (2019R1A6A3A01094872), Ministry of Science and ICT (2017R1A2B2009117, 2019M3E6A1103999, Funder Id: http://dx.doi.org/10.13039/501100003725, 2020R1A4A2002828, 2020R1A2C2014685), and Korea Institute of Science and Technology Information (K-20-L02-C10-S01).

References

[1] Barnes WL, Dereux A, Ebbesen TW. Surface plasmon subwavelength optics. Nature 2003;424:824–30.
[2] Hutter E, Fendler JH. Exploitation of localized surface plasmon resonance. Adv Mater 2004;16:1685–706.
[3] Muhlschlegel P, Eisler HJ, Martin OJF, Hecht B, Pohl DW. Resonant optical antennas. Science 2005;308:1607–9.
[4] Novotny L, van Hulst N. Antennas for light. Nat Photonics 2011;5:83–90.
[5] Lee J, Song J, Sung GY, Shin JH. Plasmonic waveguide ring resonators with 4 nm air gap and λ^2/15,000 mode-area fabricated using photolithography. Nano Lett 2014;14:5533–8.
[6] Fang N, Lee H, Sun C, Zhang X. Sub-diffraction–limited optical imaging with a silver superlens. Science 2005;308:534–7.
[7] Anker JN, Hall WP, Lyandres O, Shah NC, Zhao J, van Duyne RP. Biosensing with plasmonic nanosensors. Nat Mater 2008;7:442–53.
[8] Juan ML, Righini M, Quidant R. Plasmon nano-optical tweezers. Nat Photonics 2011;5:349–56.
[9] Atwater HA, Polman A. Plasmonics for improved photovoltaic devices. Nat Mater 2010;9:205–13.
[10] Roberts AS, Pors A, Albrektsen O, Bozhevolnyi SI. Subwavelength plasmonic color printing protected for ambient use. Nano Lett 2014;14:783–7.
[11] Lee C-H, Kim Y, Song J-H, et al. Near-ultraviolet structural colors generated by aluminum nanodisk array for bright image printing. Adv Opt Mater 2018;6:1800231.
[12] Zhang ZJ, Wang J, Chen CH. Near-infrared light-mediated nanoplatforms for cancer thermo-chemotherapy and optical imaging. Adv Mater 2013;25:3869–80.
[13] Ebbesen TW, Lezec HJ, Ghaemi HF, Thio T, Wolff PA. Extraordinary optical transmission through sub-wavelength hole arrays. Nature 1998;391:667–9.
[14] Butet J, Brevet PF, Martin OJF. Optical second harmonic generation in plasmonic nanostructures: from fundamental principles to advanced applications. ACS Nano 2015;9:10545–62.
[15] Lu BR, Xu C, Liao J, Liu J, Chen Y. High-resolution plasmonic structural colors from nanohole arrays with bottom metal disks. Opt Lett 2016;41:1400–3.
[16] Brolo AG. Plasmonics for future biosensors. Nat Photonics 2012;6:709–13.
[17] Zheng HY, Jin XR, Park JW, et al. Tunable dual-band perfect absorbers based on extraordinary optical transmission and Fabry–Perot cavity resonance. Opt Express 2012;20:24002–9.
[18] Kumar S, Wolken GG, Wittenberg NJ, Arriaga EA, Oh S-H. Nanohole array-directed trapping of mammalian mitochondria enabling single organelle analysis. Anal Chem 2015;87:11973–7.
[19] Zhang Y, Grady NK, Ayala-Orozco C, Halas NJ. Three-dimensional nanostructures as highly efficient generators of second harmonic light. Nano Lett 2011;11:5519–23.
[20] Aouani H, Navarro-Cia M, Rahmani M, et al. Multiresonant broadband optical antennas as efficient tunable nanosources of second harmonic light. Nano Lett 2012;12:4997–5002.
[21] Thyagarajan K, Butet J, Martin OJF. Augmenting second harmonic generation using Fano resonances in plasmonic systems. Nano Lett 2013;13:1847–51.
[22] Celebrano M, Wu XF, Baselli M, et al. Mode matching in multiresonant plasmonic nanoantennas for enhanced second harmonic generation. Nat Nanotechnol 2015;10:412–7.

[23] Kim MK, Sim H, Yoon SJ, et al. Squeezing photons into a point-like space. Nano Lett 2015;15:4102–7.
[24] Gennaro SD, Rahmani M, Giannini V, et al. The interplay of symmetry and scattering phase in second harmonic generation from gold nanoantennas. Nano Lett 2016;16:5278–85.
[25] Zhang S, Li GC, Chen YQ, et al. Pronounced Fano resonance in single gold split nanodisks with 15 nm split gaps for intensive second harmonic generation. ACS Nano 2016;10:11105–14.
[26] Arbore MA, Galvanauskas A, Harter D, Chou MH, Fejer MM. Engineerable compression of ultrashort pulses by use of second-harmonic generation in chirped-period-poled lithium niobate. Opt Lett 1997;22:1341–3.
[27] Imeshev G, Arbore MA, Fejer MM, Galvanauskas A, Fermann M, Harter D. Ultrashort-pulse second-harmonic generation with longitudinally nonuniform quasi-phasematching gratings: pulse compression and shaping. J Opt Soc Am B 2000;17:304–18.
[28] Bautista G, Huttunen MJ, Makitalo J, Kontio JM, Simonen J, Kauranen M. Second-harmonic generation imaging of metal nano-objects with cylindrical vector beams. Nano Lett 2012;12:3207–12.
[29] Butet J, Thyagarajan K, Martin OJ. Ultrasensitive optical shape characterization of gold nanoantennas using second harmonic generation. Nano Lett 2013;13:1787–92.
[30] Van Nieuwstadt JA, Sandtke M, Harmsen RH, et al. Strong modification of the nonlinear optical response of metallic subwavelength hole arrays. Phys Rev Lett 2006;97:146102.
[31] Moreau A, Granet G, Baida FI, van Labeke D. Light transmission by subwavelength square coaxial aperture arrays in metallic films. Opt Express 2003;11:1131–6.
[32] Saleh AA, Dionne JA. Toward efficient optical trapping of sub–10-nm particles with coaxial plasmonic apertures. Nano Lett 2012;12:5581–86.
[33] Park HR, Chen XS, Nguyen NC, Peraire J, Oh SH. Nanogap-enhanced terahertz sensing of 1 nm thick ($\lambda/10^6$) dielectric films. ACS Photonics 2015;2:417–24.
[34] Yoo D, Mohr DA, Vidal-Codina F, et al. High-contrast infrared absorption spectroscopy via mass-produced coaxial zero-mode resonators with sub-10 nm gaps. Nano Lett 2018;18:1930–6.
[35] Yoo D, Vidal-Codina F, Ciraci C, et al. Modeling and observation of mid-infrared nonlocality in effective epsilon-near-zero ultranarrow coaxial apertures. Nat Commun 2019;10:4476.
[36] Nezami MS, Yoo D, Hajisalem G, Oh SH, Gordon R. Gap plasmon enhanced metasurface third-harmonic generation in transmission geometry. ACS Photonics 2016;3:1461–7.
[37] Lee J, Sung S, Choi JH, Eom SC, Mortensen NA, Shin JH. Ultra sub-wavelength surface plasmon confinement using air-gap, sub-wavelength ring resonator arrays. Sci Rep 2016;6:22305.
[38] Canfield BK, Husu H, Laukkanen J, et al. Local field asymmetry drives second-harmonic generation in noncentrosymmetric nanodimers. Nano Lett 2007;7:1251–5.
[39] Berthelot J, Bachelier G, Song M, et al. Silencing and enhancement of second-harmonic generation in optical gap antennas. Opt Express 2012;20:10498–508.
[40] Butet J, Dutta-Gupta S, Martin OJF. Surface second-harmonic generation from coupled spherical plasmonic nanoparticles: eigenmode analysis and symmetry properties. Phys Rev B 2014;89:10.
[41] Ray PC. Size and shape dependent second order nonlinear optical properties of nanomaterials and their application in biological and chemical sensing. Chem Rev 2010;110:5332–65.
[42] Ponsetto JL, Bezryadina A, Wei FF, et al. Experimental demonstration of localized plasmonic structured illumination microscopy. ACS Nano 2017;11:5344–50.
[43] Yoon SJ, Lee J, Han S, et al. Non-fluorescent nanoscopic monitoring of a single trapped nanoparticle via nonlinear point sources. Nat Commun 2018;9:2218.
[44] Hess O, Pendry JB, Maier SA, Oulton RF, Hamm JM, Tsakmakidis KL. Active nanoplasmonic metamaterials. Nat Mater 2012;11:573–84.
[45] Sung S, Kim C-H, Lee J, et al. Advanced metal lift-offs and nanoimprint for plasmonic metal patterns. Int J Pr Eng Man-GT 2014;1:25–30.
[46] Clausen JS, Hojlund-Nielsen E, Christiansen AB, et al. Plasmonic metasurfaces for coloration of plastic consumer products. Nano Lett 2014;14:4499–504.
[47] Siegfried T, Wang L, Ekinci Y, Martin OJF, Sigg H. Metal double layers with sub–10 nm channels. ACS Nano 2014;8:3700–6.
[48] Ye F, Burns MJ, Naughton MJ. Structured metal thin film as an asymmetric color filter: the forward and reverse plasmonic halos. Sci Rep 2014;4:7267.
[49] Wang FX, Rodriguez FJ, Albers WM, Ahorinta R, Sipe JE, Kauranen M. Surface and bulk contributions to the second-order nonlinear optical response of a gold film. Phys Rev B 2009;80:4.
[50] Bachelier G, Butet J, Russier-Antoine I, Jonin C, Benichou E, Brevet PF. Origin of optical second-harmonic generation in spherical gold nanoparticles: local surface and nonlocal bulk contributions. Phys Rev B 2010;82:5.
[51] Benedetti A, Centini M, Bertolotti M, Sibilia C. Second harmonic generation from 3D nanoantennas: on the surface and bulk contributions by far-field pattern analysis. Optics Express 2011;19:26752–67.
[52] Zeman EJ, Schatz GC. An accurate electromagnetic theory study of surface enhancement factors for silver, gold, copper, lithium, sodium, aluminum, gallium, indium, zinc, and cadmium. J Phys Chem 1987;91:634–43.

Supplementary Material: The online version of this article offers supplementary material (https://doi.org/10.1515/nanoph-2020-0066).